Self-Assembly of $Co_3V_2O_8$ Multilayered Nanosheets: Controllable Synthesis, Excellent Li-Storage Properties, and Investigation of Electrochemical Mechanism

Gongzheng Yang,[†] Hao Cui,[†,‡] Guowei Yang,[†] and Chengxin Wang[†,‡,*]

[†]State Key Laboratory of Optoelectronic Materials and Technologies, School of Physics Science and Engineering, Sun Yat-sen (Zhongshan) University, Guangzhou 510275, People's Republic of China and [‡]The Key Laboratory of Low-Carbon Chemistry & Energy Conservation of Guangdong Province, Sun Yat-sen (Zhongshan) University, Guangzhou 510275, People's Republic of China

ABSTRACT Developing electrode materials with both high energy and power densities holds the key for satisfying the urgent demand of energy storage worldwide. Herein, we demonstrate the successful preparation of $Co_3V_2O_8$ nanostructures that are constructed from self-assembly of ultrathin nanosheets *via* a simple hydrothermal method followed by annealing in air at 350 °C for 2 h. A "slipping—exfoliating—self reassembly" model based on the time-dependent experiments was proposed to elucidate the formation of the hierarchical nanosheets. When tested as lithium ion anodes, the as-synthesized multilayered nanoarchitectures exhibit outstanding reversible capacity (1114 mA h g^{-1} retained after 100 cycles) and excellent rate performance (361 mA h g^{-1} at a high current density of 10 A g^{-1}) for lithium storage. Detailed investigations of the morphological and structural changes of $Co_3V_2O_8$ upon cycling reveal an interesting kinetics toward lithium ion intercalations, where reversible conversion reactions between Co and CoO are found proceeding on the amorphous lithiated vanadium oxides matrixes. We believe that this observation is a valuable discovery for metal vandates-based lithium ion anodes. The superior electrochemical performances of the multilayered $Co_3V_2O_8$ nanosheets can be attributed to the unique morphologies and particularly the surface-to-surface constructions that are generated during the lithium ion insertion processes.

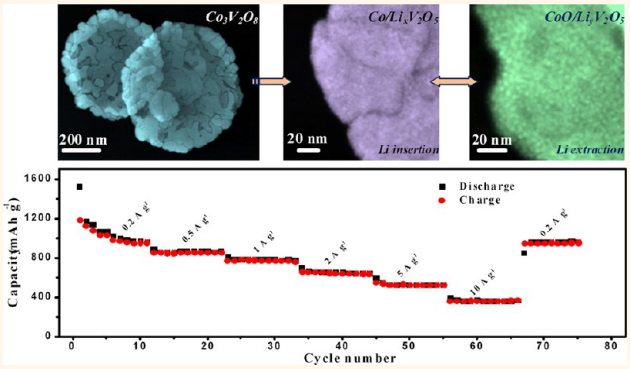

KEYWORDS: $Co_3V_2O_8$ · self-assembly · nanosheets · lithium ion battery anodes · excellent Li-storage property · electrochemical mechanism

Nowadays, transition metal oxides have attracted much attention because of their relatively low cost, environmental benignity, higher theoretical capacity, and safety as anode materials applicable for lithium ion batteries.[1−5] However, their practical applications are still hindered by the poor stability that is caused by the drastic volume change and reduced crystallinity of the active materials with prolonged cycling. Downsizing materials to nanoscale level has been proved as an effective approach to enhance the electrochemical performance due to the increased surface areas and the shortened lithium ion diffusion paths.[6−9] However, what remains challenging to date is how to prevent the aggregation of the pulverized nanograins that emerges during the lithium ion insertions. Hence, many innovative architectures were developed to address this problem, such as York-shell hollow spheres,[10−12] carbon-coating,[13−17] and three-dimensional frameworks.[18−20] Among them, two-dimensional (2D) nanoarchitectures based on the surface-to-surface "binding" between the graphene nanosheets and active materials are of particular interest.[21−28] In such a structure, the isolated metal oxide quantum dots anchored tightly on the graphene

* Address correspondence to wchengx@mail.sysu.edu.cn.

Received for review December 17, 2013 and accepted March 31, 2014.

Published online March 31, 2014
10.1021/nn406449u

nanosheets can effectively prevent the volume expansion associated with the lithium insertion process, which is favorable to high capacity as well as cycling stability.[29] Unfortunately, tedious procedures or expensive additives (graphene) are universally introduced to the final products, and consequently it is necessary to find relatively simple/low-cost ways to produce the 2D electrodes with satisfactory high capacity and high rate capability.

Superior to single-phase oxides, mixed metal oxides can synergistically improve the electrochemical properties including electrical/ionic conductivity, reversible capacity, and mechanical stability.[30] Recently, a few studies have reported the syntheses of double metal oxide micro/nanostructrues and evaluated their lithium storage properties as negative electrodes with encouraging results. For example, Le *et al.* reported the fabrication of hierarchical $Co_xMn_{3-x}O_4$ array micro/nanostructures with tunable morphologies, which can deliver remarkable specific capacities (540−207 mA h g^{-1}) at various current rates (1−10 C) and good cycling stability for highly reversible lithium storage.[30] Yogesh Sharma and co-workers had developed nanophase $ZnCo_2O_4$ as high performance anodes, in which both Zn and Co ions act as mutual beneficial matrixes, and reversible capacity contribution of Zn through both alloy formation and displacement reaction takes place to yield stable and high capacities.[31] In addition, Cherian and co-workers recently synthesized continuous $NiFe_2O_4$ nanofibers by an electrospinning approach. The nanofibers exhibited a high charge-storage capacity of 1000 mA h g^{-1} even after 100 cycles with a high Coulmbic efficiency of 100% between 10 and 100 cycles.[32] However, as important mixed-metal oxides, metal vanadates seem to be an unnoticed group using as lithium ion anodes. The early research on the vanadates as lithium ion anodes can be traced back to Denis's work in 1999.[33,34] Numerous classes of vanadates, such as $Co(VO_3)_2$, $Co_2V_2O_7$, $LiNiVO_4$, and RVO_4 (R = In, Cr, Fe, Al), were tested for their electrochemical properties *versus* lithium. The best results were obtained for the α-$Co(VO_3)_2$ phase, which can reversibly react with as high as 9.5 Li^+ with only 17% irreversible capacity.[33,34] Despite these inspiring features, to date, their reactivity kinetics toward lithium intercalations and theoretical capacities are not clearly investigated. Taking the fast capacity fading upon charge−discharge into account, there are only a few reports on the application of metal vanadates for lithium ion anodes.[6,35−37]

In the present work, we have reported for the first time the successful preparation of the $Co_3V_2O_8$ nanostructures, which exhibit a unique multilayered architecture that is constructed from the self-assembly of ultrathin nanosheets. The measurements of $Co_3V_2O_8$ as lithium ion anodes are carried out, and corresponding results show that the as-synthesized products have manifested all the merits of an ideal electrode material: high capacity (initial discharge capacity: 1380 mA h g^{-1}), long life span (96% of the second cyclic discharge capacity retained after 100 cycles), and fantastic rate capability (361 mA h g^{-1} at a high current density of 10 A g^{-1}). Moreover, detailed investigations of the morphological and structural changes of the $Co_3V_2O_8$ nanosheets upon cycling help us to better understanding their electrochemical behaviors. Astonishingly, completely reversible conversion reactions between metallic Co quantum dots and CoO nanoparticles on the amorphous lithiated vanadium oxide nanosheets were observed since the first discharge process. The newly generated 2D surface-to-surface structure, similar to the graphene-based 2D architecture, can efficiently accommodate the volume change and thus prevent pulverization of the electrode. Meanwhile, the strongly coupled Co- and V-oxides may also be conductive to enhance the electrochemical performances. As a result, the self-assembly of $Co_3V_2O_8$ multilayered nanosheets is proposed as a promising anode candidate for lithium ion batteries.

RESULTS AND DISCUSSION

Structure and Morphology. Figure 1A,B present the typical SEM images of the as-synthesized samples after annealing in air at 350 °C for 2 h, from which one can clearly see that the samples exhibit uniform sheet-shaped morphology. Wave-like diffraction contrast in the low-magnification TEM images (Figure 1C,D) implies the unique microstructure of the products. EDS results in Figure 1E demonstrate that the nanosheets are composed of the elements Co, O, and V. Element mapping characterizations were carried out to further investigate the internal structure of the samples. As shown in Figure 1F, an unexpected completely novel picture is seen: such an integral nanosheet is actually made up of many fragments. In contrast, a highly homogeneous distribution of the elements reveals the high purity of the products. Hence, XRD and high-resolution TEM (HRTEM) experiments were performed to reveal the crystal structure of the peculiar architectures. All intense peaks shown in Figure 1G can be well indexed to cubic $Co_3V_2O_8$ (JCPDS No. 16-0675). To the best of our knowledge, this is the first time the successful preparation of a $Co_3V_2O_8$ nanostructure has been reported. Furthermore, the HRTEM image of a crystalline $Co_3V_2O_8$ nanosheet in Figure 1H displays a basal space of 0.251 nm, which is in good agreement with the (311) lattice fringe of the crystalline $Co_3V_2O_8$. However, there are more than one set of selected area electron diffraction (SAED) spots collected from the nanosheet, further indicating the multilayered feature of the $Co_3V_2O_8$ nanosheets. Figure S1A (Supporting Information) exhibits a representative TEM image of the harvested samples in solution before calcination, where no significant difference can be detected compared with the calcined $Co_3V_2O_8$ nanosheets. The hexagonal SAED spot in Figure S1B suggests a similar

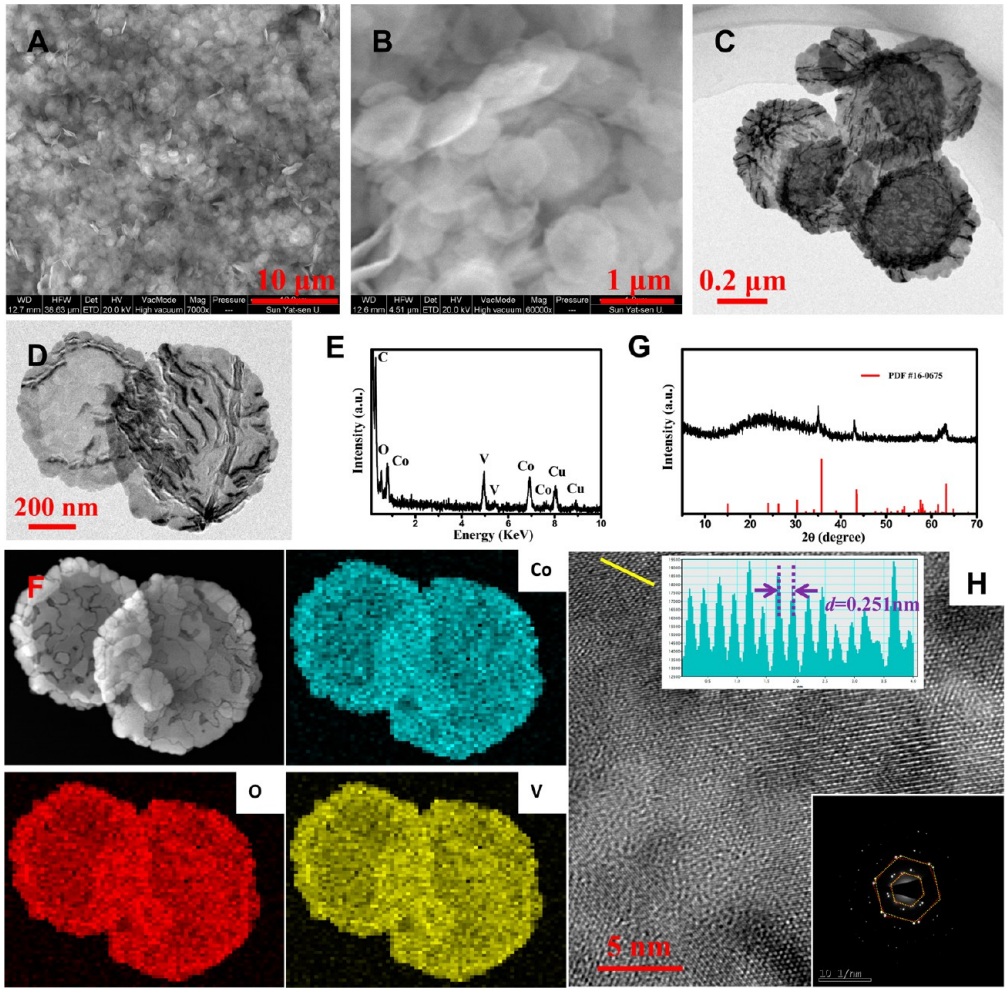

Figure 1. Structural characterizations of the $Co_3V_2O_8$ nanosheets. (A, B) SEM and (C, D) TEM images of $Co_3V_2O_8$ nanosheets. (E) Representative EDS spectrum. (F) Scanning TEM (STEM) and element mapping images of the $Co_3V_2O_8$ nanosheets in (D). (G) XRD pattern. (H) HRTEM image of an individual nanosheet. The insets in (H) show the measurements of the crystal interfaces and corresponding SAED pattern.

crystalline structure to the cubic $Co_3V_2O_8$. However, the distinguishing HRTEM and XRD results (Figure S1C,D) reveal that a phase change has occurred during the calcination process. Therefore, the phase of the products synthesized in solution is speculated to be $Co_3V_2O_8 \cdot nH_2O$.

Formation Mechanism. To understand the growth mechanism of these nanosheets, time-dependent experiments were carried out. As shown in Figure 2, the samples collected at four different stages present totally different morphologies. At the preliminary stage, hexagonal nanosheets with a perfect outline constitute the major part of the products (Figure 2A,E). As the reaction time is increased to 1 h, a lot of thinner nanosheets seem to peel off from the matrix (see the region indicated by the arrow, Figure 2F), while the reduced nanosheet looks much more transparent, accompanied by the appearance of jagged edges. In addition, shown in Figure 2B, one can see that there is a considerable amount of hexagonal nanosheets remaining in the products, implying that the reaction is far from over. Then, samples similar to the final products were obtained after the reaction time was extended to 3 h (Figure 2C,G), except for some nanoparticles still lying on the nanosheet. So far, we speculate that the final multilayered structure might be derived from the continuous peeling of the preliminary hexagonal matrix. Just as expected, the multilayered nanosheets composed of many fragments with distinct boundaries were successfully prepared as the reaction time was increased to 6 h (Figure 2D,H). However, it is obvious that common to all the samples collected at the four stages (Figure 2A–D) is the uniformity of the morphologies. By comparison with the uniform nanosheets in Figure 1A, we can conclude that the architectures of the products are entirely controlled by the reaction time.

Furthermore, if we could probe the variations of the thickness of the samples, it would help us to better understand the growth processes during the synthesis. Therefore, atomic force microscope (AFM) studies were introduced to examine the changes, and the corresponding results are shown in Figure 3. Figure 3A–C

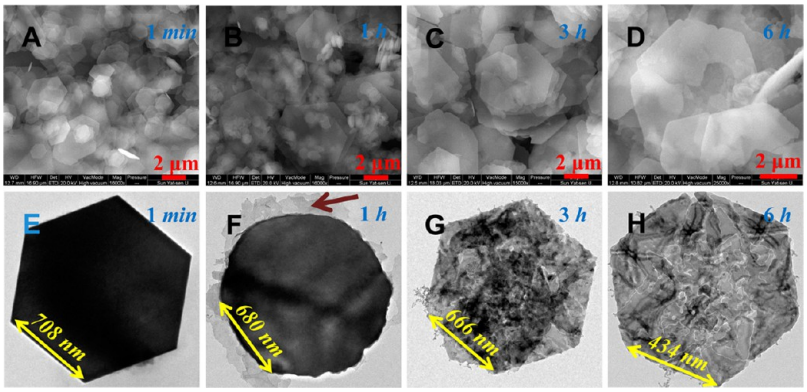

Figure 2. Typical SEM and TEM images of the products obtained in solutions at various stages. (A, E) 1 min. (B, F) 1 h. (C, G) 3 h. (D, H) 6 h.

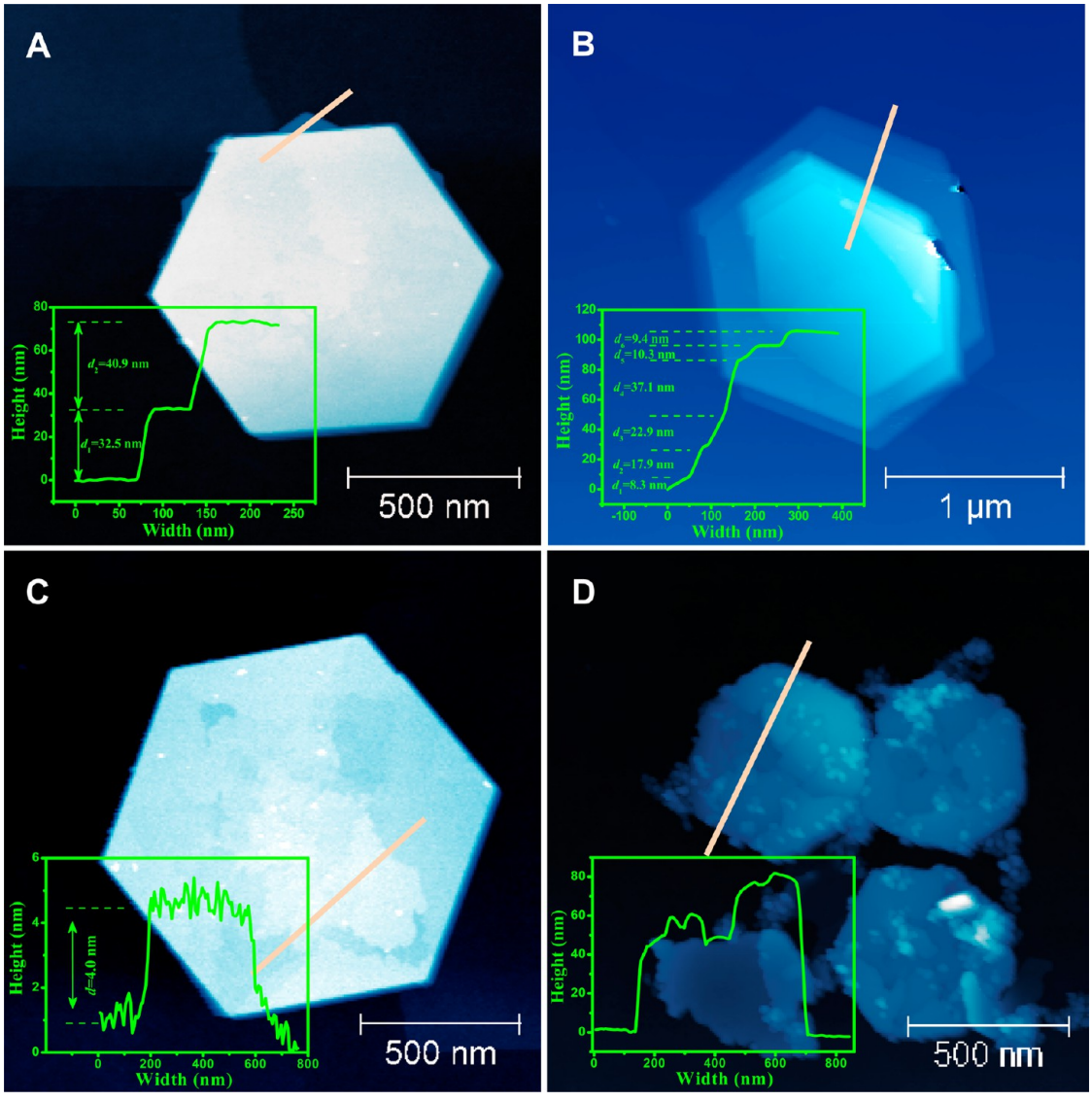

Figure 3. AFM images of the products obtained in solutions. (A–C) 1 min. (D) 12 h. The insets show the "height–width" profiles corresponding to the lines marked with yellow in the AFM images.

present the typical AFM images of products obtained at 1 min. Two overlapped nanosheets in Figure 3A display the same standard geometric configuration but different thicknesses. Meanwhile, multilayered nanosheets with distorted hexagonal shapes (Figure 3B) were also prepared in the solution, where each upper

nanosheet was observed slightly slipping from the lower matrix. The existence of so many dislocations demonstrates that the hydrothermal reaction proceeded very quickly at the very beginning, with the result of the emergence of slices that possess a thickness of ~4 nm on the surface of the nanosheets (Figure 3C). Figure 3D exhibits an AFM image of the final products, where the fragments might be generated from the ultrasonic process during the sample preparation. The hilly height curve of the nanosheets further signifies the multilayered nature of the products, which matches well with the STEM and SAED results. On the basis of the above observations, a "slipping−exfoliating−self reassembly" model was proposed to elucidate the formation of the unique hierarchical nanosheets, as shown in Figure 4. It is well known that crystalline H_2O might occupy the interlayer spaces between the $[VO_x]$ polyhedron skeleton and plays a critical role in the growth of vanadium oxide-based compounds.[38] In this study, the $Co_3V_2O_8 \cdot nH_2O$ hydrate with a layered structure is first formed under the hydrothermal conditions. As the reaction continues, the interactions between the layers of the $Co_3V_2O_8 \cdot nH_2O$ hydrate are weakened, and the $Co_3V_2O_8 \cdot nH_2O$ layers gradually slip from the matrix to form a staircase-like morphology. Subsequently, in order to release the strong stress and lower the total energy, "an exfoliating process" occurs in which the $Co_3V_2O_8 \cdot nH_2O$ layers split into irregular smaller blocks. Similar models for the formation of nanostructures from layered compounds have also been reported.[39,40] Finally, when all the $Co_3V_2O_8 \cdot nH_2O$ hydrate is shortened to thin slices, the multilayered architectures will grow due to surface adsorption.

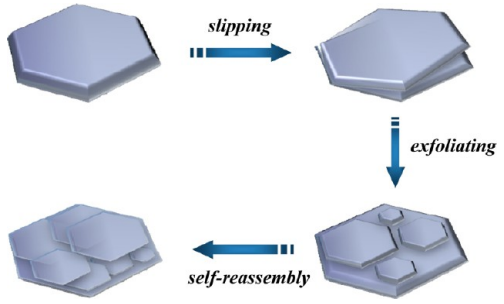

Figure 4. Schematic illustration of the possible growth processes of the multilayered nanosheets.

Electrochemical Properties. Noticing the evolution of the $Co_3V_2O_8$ nanostructures with reaction time, we selected the annealed hexagonal blocks (precursors synthesized at 1 min) and the final multilayered nanosheets (annealed, precursors synthesized at 12 h) as the electrode materials for detailed investigation of the electrochemical performances, which are marked with 1 min and 12 h, respectively. Figure 5A,C show the cyclic voltammogram (CV) curves obtained at a scan rate of 0.2 mV s^{-1} in the potential window of 2.5 V to 10 mV. By careful observation, one can see that both the samples exhibit the same CV curves, implying their identical electrochemical behaviors. Figure 5B,D display their discharge−charge profiles at the current density of 1 A g^{-1}. The initial discharge capacities of both the electrodes were 1500 and 1380 mA h g^{-1}, which are equivalent to an intercalation of approximately

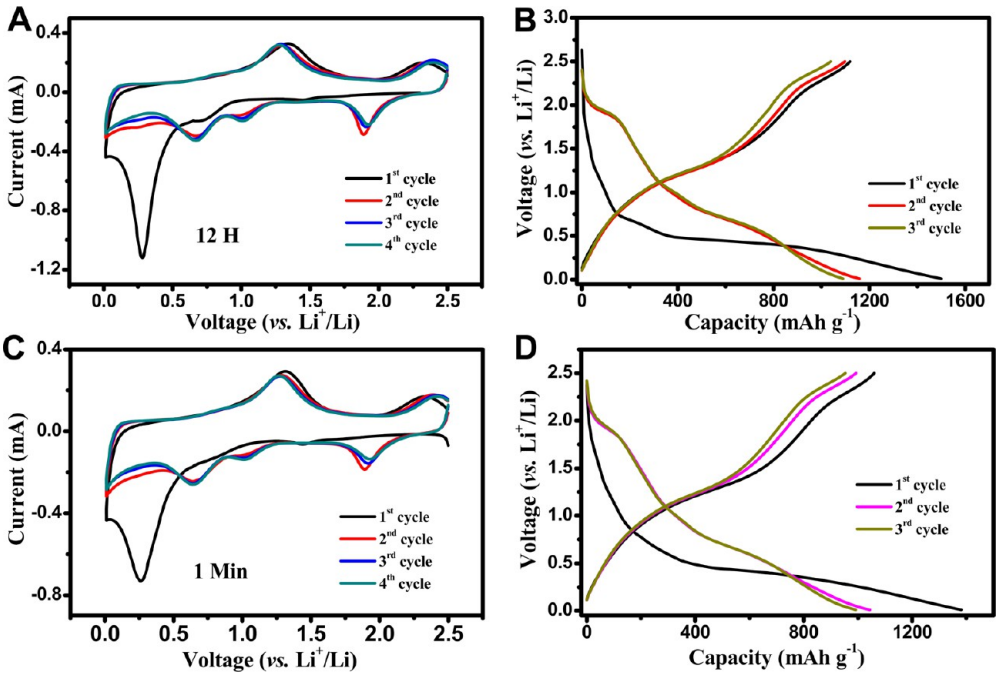

Figure 5. CV curves and charge/discharge profiles of the $Co_3V_2O_8$ nanosheets obtained at (A, B) 12 h and (C, D) 1 min, respectively.

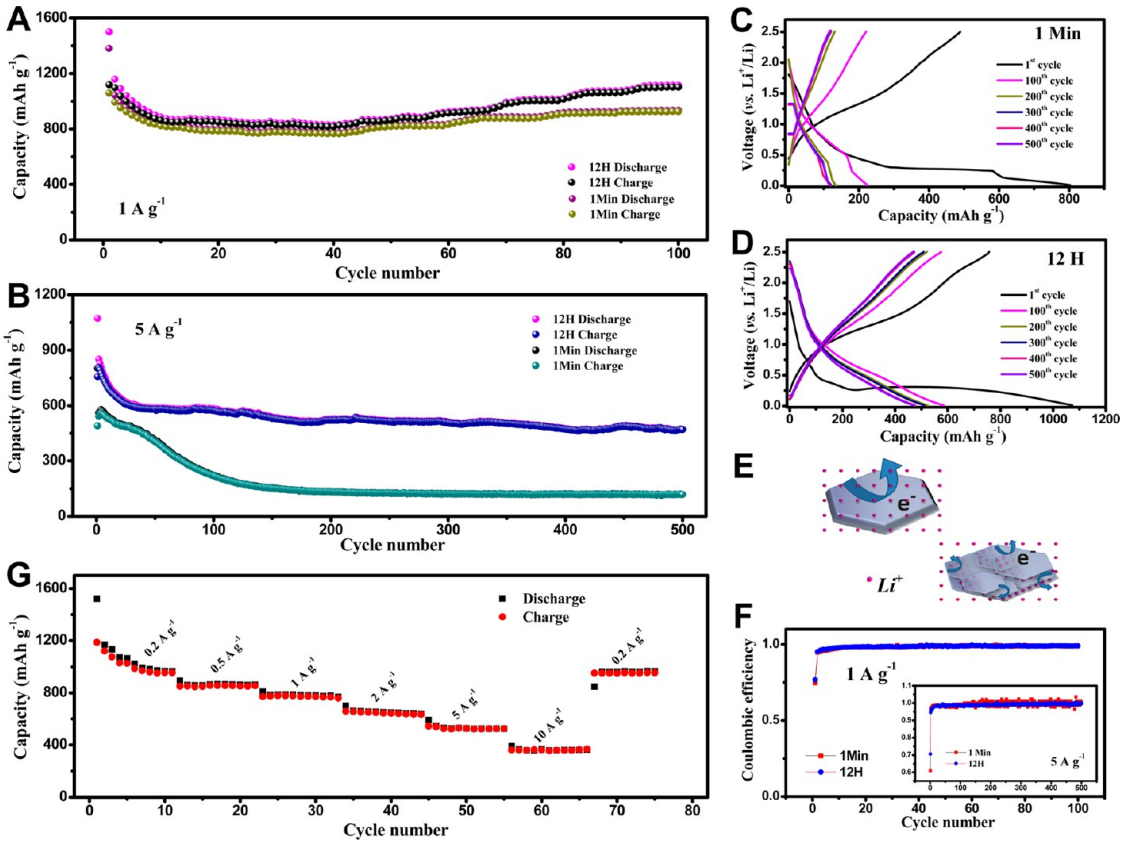

Figure 6. Electrochemical performances of the $Co_3V_2O_8$ nanosheets. (A, B) Reversible charge/discharge capacities against cycle number for samples obtained at 1 min and 12 h at different current densities of 1 and 5 A g^{-1} in the voltage window of 0.01−2.5 V. (C, D) Corresponding charge/discharge profiles in the first, 100th, 200th, 300th, 400th, and 500th cycles of the samples 1 min and 12 h at the current density of 5 A g^{-1}. (E) Schematic illustration of electron-transfer pathways for two samples. (F) Corresponding Coulombic efficiencies. (G) Rate performance of the $Co_3V_2O_8$ nanosheets obtained at 12 h.

22.7 and 19.7 Li per formula unit according to the Faraday equation. These values are considerably higher than those achieved in other oxides that have attracted great attentions so far (*e.g.*, ∼2.0 Li for CoO,[29,41,42] ∼4.4 Li for SnO_2,[43] and ∼6.0 Li for Fe_2O_3[44,45]). Moreover, remarkable reversible capacities of 1120 and 1060 mA h g^{-1} can be achieved, indicating fewer side-reactions and excellent cycle stabilities.

The cycle performances of both the electrodes at different current densities are compared in Figure 6A,B, from which we can see that the multilayered nanosheets give a better performance. Actually, at a lower rate of 1 A g^{-1}, both the samples show a comparable cycling stability that is 96% and 90% of the capacity that is retained after 100 cycles compared with the second cycle for the anodes of 12 h and 1 min, respectively. However, a completely opposite result arises as the current density increases to 5 A g^{-1}, as shown in Figure 6B. The multilayered nanosheets exhibit a splendid cycle performance, where a capacity as high as 470 mA h g^{-1} can be achieved even after 500 cycles, corresponding to an intercalation of ∼7.2 Li in the compounds. For the integral hexagonal blocks (1 min), it is observed that within 60 cycles, their discharge capacities decayed to 370 mA h g^{-1}, which is close to the theoretical capacity of graphite, and rapidly faded below 120 mA h g^{-1}. Figure 6C,D present the voltage capacity profiles associated with a charge−discharge rate of 5 A g^{-1} of both electrodes.

As we known, lithium ion technologies suffer from kinetic problems linked to the solid-state diffusion of Li, the conductivity of the electrolyte, and the quality of interfaces.[2] Downsizing the active materials to the nanoscale has been proved an effective way to enhance the kinetics since it can provide short diffusion lengths for lithium ions and consequently improve the rate capability of the electrodes. As illustrated in Figure 6E, much more exposed interfaces of the multilayered nanosheets that are generated from the continuous peeling of the hexagonal blocks will greatly increase the lithium ion diffusion and electronic conduction and thus lead to a better rate stability. More convincing evidence for the enlarged interfaces was characterized by the nitrogen adsorption/desorption analyses. A high surface area of 39.4 m^2 g^{-1} is recorded for the multilayered architectures (Figure 7C), which is larger than the samples synthesized at 1 min (Figure 7A). Besides, it is worthy of noticing that the adsorption of the nitrogen is mainly centralized at the narrow pressure of 0.5−0.8 for both the products,

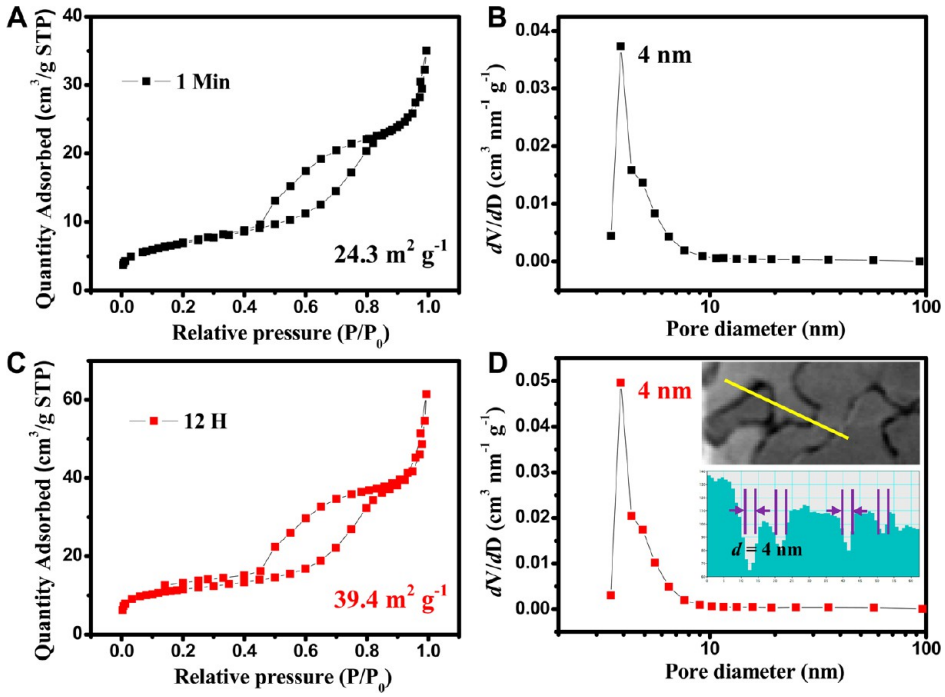

Figure 7. Nitrogen adsorption isotherms and respective pore size distributions of the calcined samples obtained at (A, B) 1 min and (C, D) 12 h. The insets in (D) show the magnified TEM images of an individual nanosheet and the measurements of the channels.

indicating the relative uniformity of the pore diameter distribution. The corresponding density functional theory (DFT) pore size distributions in Figure 7B,D verify the uniform pore structure that concentrates at 4 nm. Together with the STEM data presented in the inset of Figure 7D, the uniform mesopores can be accounted for by the empty channel voids that occur during the self-reassembly of the constituent fragments to the multilayered nanosheets. The same pore size distribution was obtained for the samples prepared at 1 min, which might be attributed to the existence of a small amount of multilayered architectures that grow up at the very beginning.

Figure 6F gives the Coulombic efficiencies of both the electrodes that are calculated from the discharge and charge capacities at different current densities, from which one can clearly see the superior cycling performance of the multilayered $Co_3V_2O_8$ nanosheets. The rate performance of the multilayered architectures was also studied and is illustrated in Figure 6G. The result reveals that the multilayered $Co_3V_2O_8$ electrodes can provide not only high energy densities but also high power densities. Thus, we have demonstrated that the unique constructions of the novel multilayered $Co_3V_2O_8$ nanosheet make it a promising candidate as a lithium ion anode material. However, the lack of the reaction mechanism of the lithium intercalation into the metal vanadates motivates us to continue our research.

Electrochemical Reaction Mechanism. The evolutions of the morphological and structural changes of the electrodes (12 h, multilayered $Co_3V_2O_8$ nanosheets) were studied at various stages of the reduction and oxidation processes by means of TEM analyses. Here we report the results on the first cycle and the 10th cycle of the electrode materials (black solid dots in Figure 8 and Figure 9).

Figure 8B presents a low-magnification TEM image of electrodes obtained at the middle of the discharge (stage 1), while the sheet-shaped constructions in the STEM image (Figure 8C) of the selected area suggest a similar architecture to the precursors. Moreover, the regular lattice fringes in the HRTEM image (Figure 8D) of such an electrode demonstrate the integrity of the constituent nanosheets of the electrodes. However, the distorted SAED pattern (inset in Figure 8D) implies the disordered tendency of the crystal structure upon cycling. Besides, the interlayer distances of 0.246 nm can be ascribed to the CoO (111) plane, indicating that the electrodes have changed from $Co_3V_2O_8$ to CoO. As the electrodes are reduced to 0.3 V (stage 2), the initial nanosheets are observed to transform into numerous quantum dots that scatter on an amorphous matrix (Figure 8E,F). The locally enlarged HRTEM image in Figure 8G shows two equal interdistances of 0.204 nm, implying that the quantum dots consist of metallic Co, combined with its FFT pattern shown in the inset of Figure 8G. Subsequently, for the third and fourth step in the oxidation process, both the electrodes depict the same morphologies (Figure 8H,I) where many homogeneously distributed nanoparticles are detected anchored on an amorphous sheet-shaped substrate.

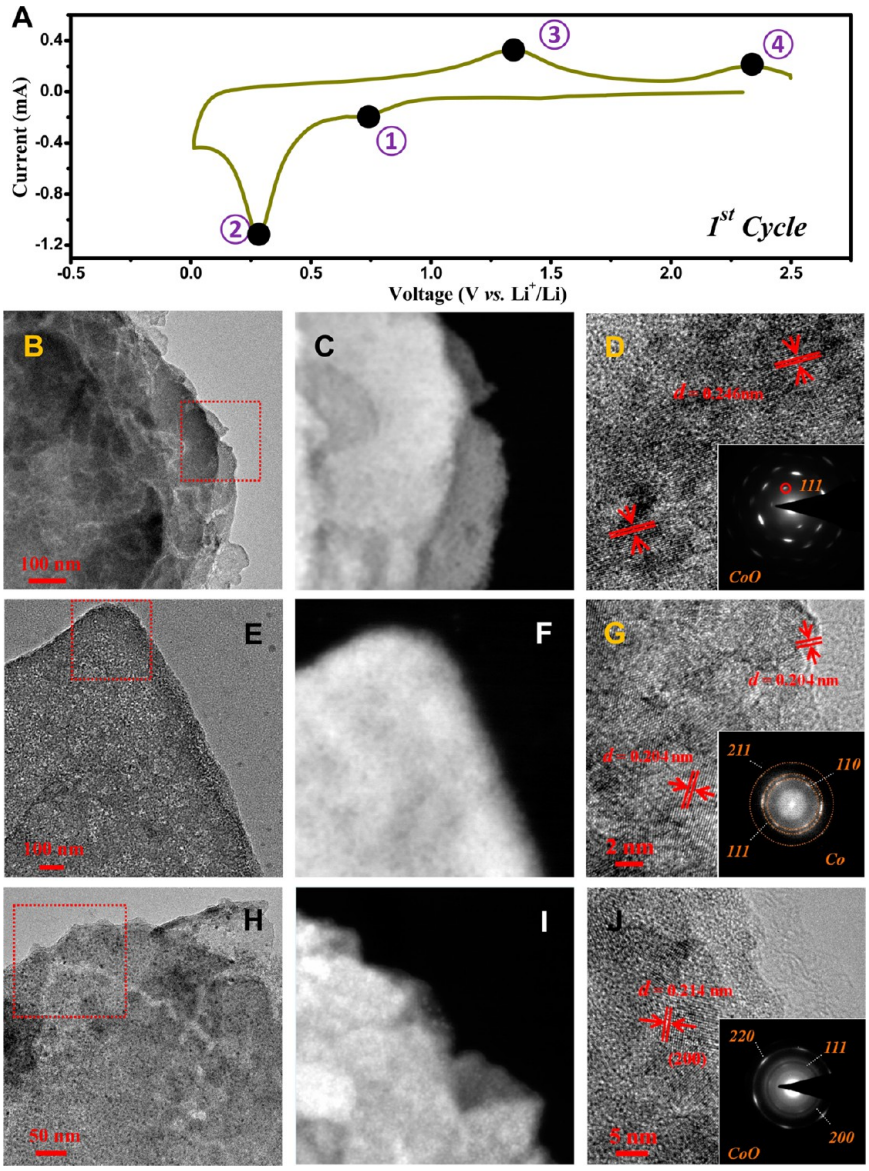

Figure 8. TEM studies of the $Co_3V_2O_8$ nanosheet (12 h) electrodes recovered from $Co_3V_2O_8$/Li cells at the first cycle. (A) Voltage–composition trace for $Co_3V_2O_8$/Li cells cycled between 0.01 and 2.5 V; the cutoff voltage of each sample studied is symbolized by an Arabic number. (B, E) TEM images realized on the reduced electrodes collected from points 1 and 2. (H) Representative TEM image of the reoxidized electrodes collected from points 3 and 4, while both the electrodes give the same morphology. (C, F, I) STEM and (D, G, J) HRTEM images corresponding to selected areas in (B, E, H), respectively. The insets in (D, G, J) show the SAED patterns.

The HRTEM image in Figure 8J of an individual nanoparticle displays a clear crystal lattice with a spacing of 0.214 nm, corresponding to the CoO (200) plane. The SAED patterns collected from the same areas exhibit a set of diffraction rings that can be assigned to the diffractions of the {111}, {200}, and {220} planes of the cubic CoO, which suggests that the metallic Co is oxidized to CoO during the delithiation process.

On the basis of the CV results, we have noticed the different electrochemical behaviors between the first cycle and the subsequent discharge/charge processes. Hence, to obtain a better insight into the morphological and structural changes on cycling, we performed *ex situ* TEM observations of the electrode materials that are collected from the six stages of the 10th cycle, as shown in Figure 9. During the lithium intercalation, three cathodic peaks are observed at 2.0, 1.0, and 0.7 V, respectively. TEM images in Figure 9A,B display the morphologies of the first two stages of lithium intercalation (2.0 and 1.0 V), where one can see that constructions similar to those in Figure 8G have been obtained. Corresponding HRTEM images (Figure S2A,B, Supporting Information) reveal that the nanoparticles consist of cubic CoO. Upon further lithiation of the electrodes, the incoming lithium ions continuously pulverize the nanoparticles into numerous quantum dots (Figure 9C,D), which were subsequently illustrated as metallic Co by the HRTEM measurements (Figure S2C,D). For the

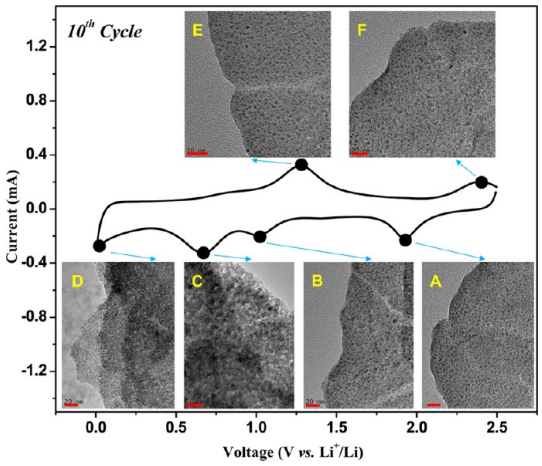

Figure 9. TEM studies of the $Co_3V_2O_8$ nanosheet (12 h) electrodes recovered from $Co_3V_2O_8$/Li cells at the 10th cycle. The cutoff voltage of each sample studied is symbolized by a black dot. (A−F) Typical TEM images obtained at the cutoff voltages of 2.0, 1.0, 0.7, 0.01, 1.3, and 2.4 V, respectively. Scale bars: 20 nm.

extraction of lithium from the electrodes, two anodic peaks are observed at 1.3 and 2.4 V, while the morphologies and structures are also found analogous to the first cycle (Figure 9E,F).

So far, a typical conversion reaction between CoO and Co has been clearly demonstrated. As we know, the conventional conversion reaction universally involves a large volume expansion and the aggregation of pulverized nanoparticles, which will significantly affect the cycling performances of the electrodes. The volume of the CoO crystal after lithium insertion is increased to 180% of the initial volume ($CoO + 2Li \leftrightarrow Co + Li_2O$; $\rho CoO = 6.345$ g/cm^3, $\rho Li_2O = 2.1$ g/cm^3, $\rho Co = 8.788$ g/cm^3, and the volume of Li was ignored).[46] Such a large volume expansion ratio will easily lead to an irreversible capacity loss and a poor cycling stability. Fortunately, looking back to the above TEM results, we can see that the morphological changes of the $Co_3V_2O_8$ upon cycling are completely reversible. Especially, all the reactions proceed on the amorphous matrix, which not only functions as the reaction sites but also serves as the separator, preventing the agglomeration of the nanograins. Consequently, the morphologies of the multilayered $Co_3V_2O_8$ nanosheets can be well preserved during the lithium intercalation, which is beneficial to the cycling stability, as shown in Figure S3 (Supporting Information). However, one question can be easily proposed: what is the role of vanadium in the lithium insertion/deinsertion processes? Accordingly, precise distributions of the elements Co, O, and V collected at three representative stages (full deinsertion (2.5 V), half-insertion (1.0 V), and full insertion (0.01 V)) were examined by the EELS characterizations. Figure 10 shows the panoramic element mapping images of the electrode materials. The uniformly dispersed components of Co and O in the three samples match well with the above TEM analyses and further confirm the conversion reaction kinetics. Most importantly, the homogeneous distributions of V suggest that the amorphous matrixes are composed of lithiated vanadium oxides.

Thus, one plausible mechanism based upon the above results was proposed to address the electrochemical behaviors of the multilayered $Co_3V_2O_8$ nanosheets, as depicted in Figure 11. At the beginning of the first cycle, the crystal structures of $Co_3V_2O_8$ are gradually destroyed, accompanied by the emergence of CoO particles that are lying on the remaining disordered lithiated cobalt metal oxide ($Li_xCo_3V_2O_8$) nanosheets. Upon further insertion of lithium ions, these CoO particles are reduced to metal Co quantum dots that are anchored on the amorphous $Li_xV_2O_5$ matrixes. Upon recharging, the metal Co quantum dots are *in situ* reoxidized to the CoO nanoparticles. During the subsequent lithium insertion/deinsertion processes, the conversion reactions between the CoO nanoparticles and Co quantum dots are completely reversible, which occurs on the amorphous $Li_xV_2O_5$ matrixes. Additionally, the redox couples at each corresponding oxidation and reduction are specified to help us better understand the electrochemical mechanism, as illustrated in Figure S4 (Supporting Information).

In addition to the encouraging results on $Co_3V_2O_8$, we observed very unusual morphologies of the electrode materials that were collected at 0.01 V (10th cycle) when discharging at a relative high current density of 1 A g^{-1}. As can be seen in Figure 12A, many irregular nanoparticles with a size of 20−100 nm (much larger than the Co quantum dots obtained at a smaller current density) are detected on the matrix, while the corresponding STEM image in Figure 12B helps us to gather more details. EDS microanalyses on the selected areas are displayed in Figure 13B. The dispersive irregular nanoparticles (point 1) consist of mostly Co as well as a few O elements, whereas the matrix (point 2) consists of Co, V, and O elements. The TEM image in Figure 12D shows many slender parallel bands arranged alternately in the selected nanoparticle (the red loop in Figure 12C). The magnified HRTEM image (Figure 14A) exhibits two distinctive lattice fringes: the narrow spacing of 0.204 nm matches well with the (111) plane of Co metal, and the other corresponds to interplanar distances of the $CoO_{(200)}$ (0.214 nm), indicating that these nanoparticles are made up of both Co and CoO. XPS spectra in Figure S5 (Supporting Information) further verify the oxidation states of such electrode materials.

The interesting findings demonstrate for the first time the electrode morphologies of the conversion reactions, and the corresponding schematic representation of the particular architecture CoO/Co/CoO/Co/CoO based on the TEM observations is presented in Figure 14C. Earlier, Dalverny *et al.* predicted a similar electrode construction according to a multi-interface

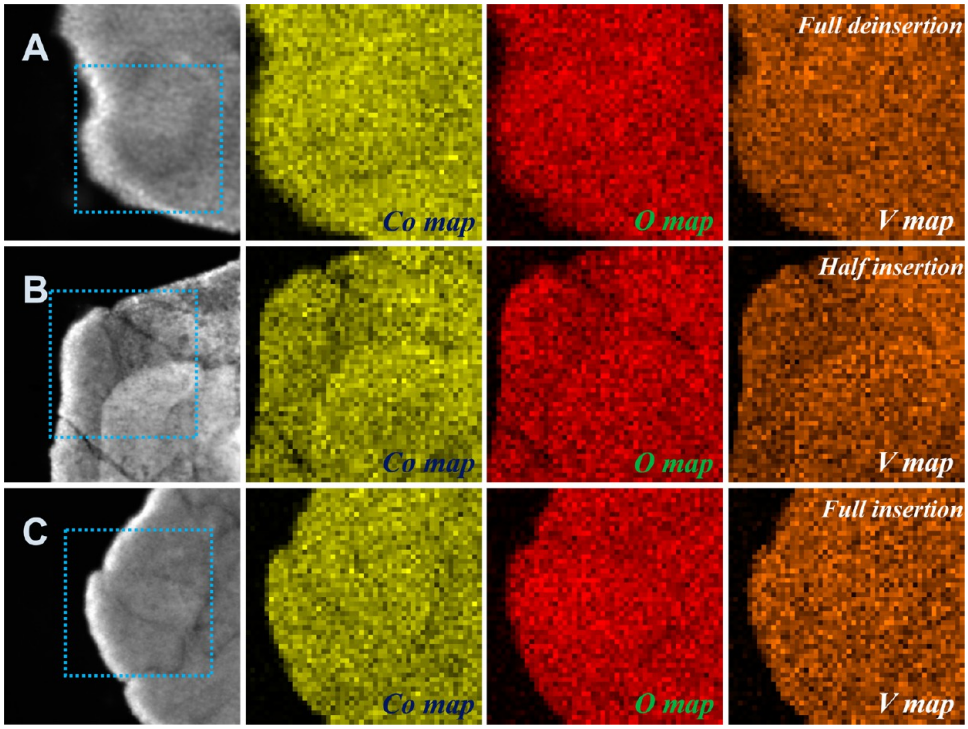

Figure 10. STEM and element mapping images of the $Co_3V_2O_8$ nanosheet (12 h) electrodes obtained at (A) 2.5, (B) 1.0, and (C) 0.01 V at the 10th cycle, respectively.

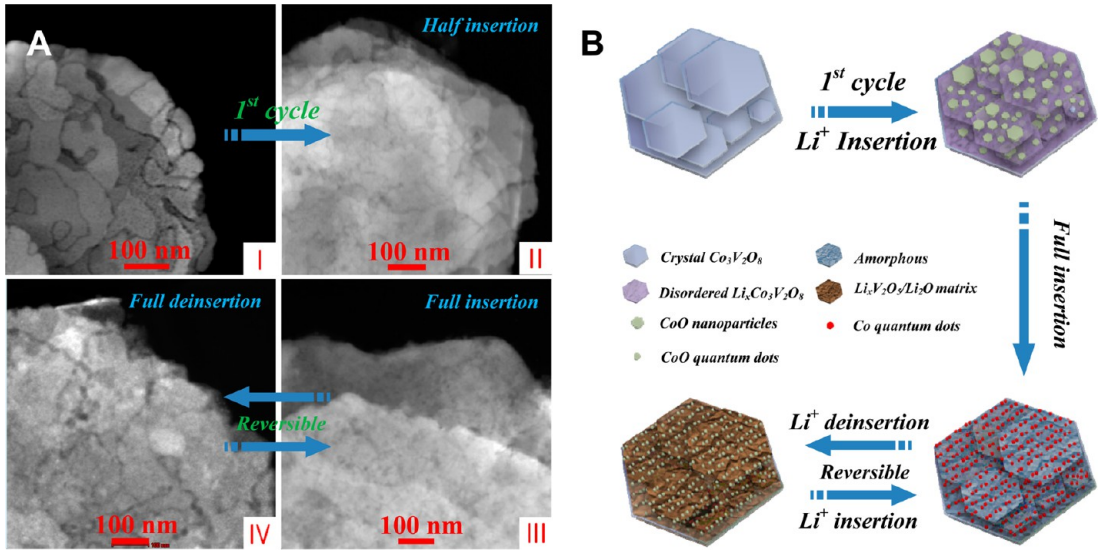

Figure 11. (A) STEM images of the $Co_3V_2O_8$ nanosheet (12 h) electrodes obtained at various stages. (B) Schematic illustration of the possible electrochemical behaviors.

superlattice approach.[47] By comparison, we can see that the biggest difference between the experimental results and the theoretical model is the formation of the sequential CoO/Co interfaces of the $Co_3V_2O_8$ electrodes (a more precise description of the CoO/Co interfaces can be seen in Figure S6). As shown in Figure 14B, there must be some special correlation between the CoO (200) and Co (111) planes upon the lithium insertions. This phenomenon has not yet been observed, while a clear explanation of this issue will help us to better understand the conversion reactions, and a further investigation is under way in our group. In addition, compared with the pure metallic Co quantum dots obtained at a small current density, the coexistence of the CoO and Co in the single nanoparticle suggests the insufficient usage of the active materials, which is the essential reason for the relatively low specific capacities of the electrodes when cycling at a high current density. Moreover, it is worthy of noticing that the capacity first decreased and then increased

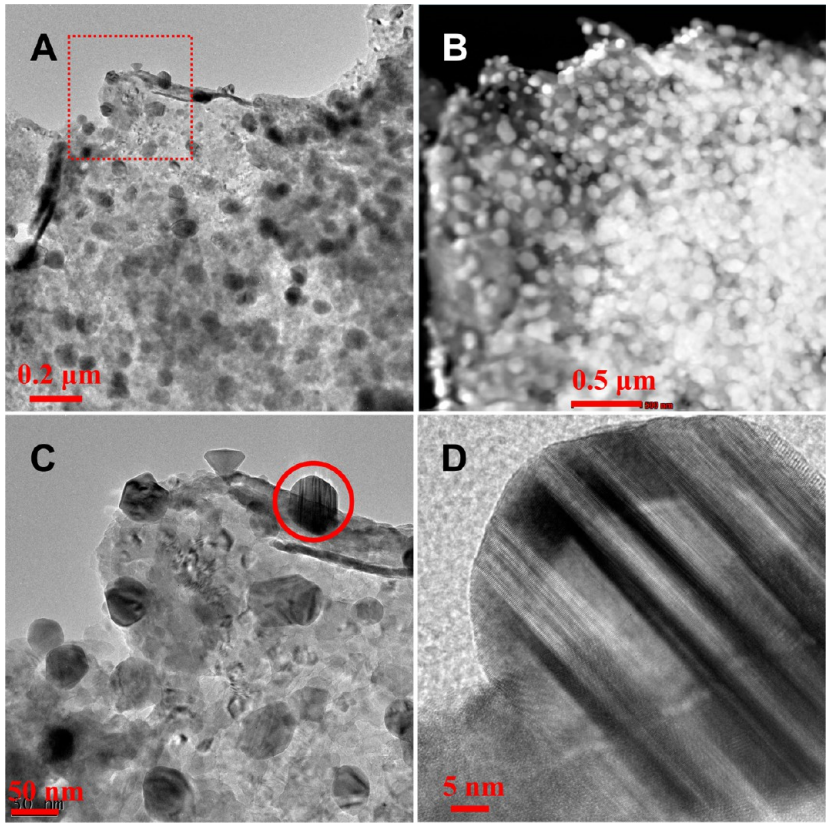

Figure 12. Structural studies of the $Co_3V_2O_8$ nanosheet (12 h) electrodes collected at a cutoff voltage of 0.01 V when discharged at a high current density of 1 A g^{-1}. (A, C, D) TEM images. (B) Corresponding STEM image.

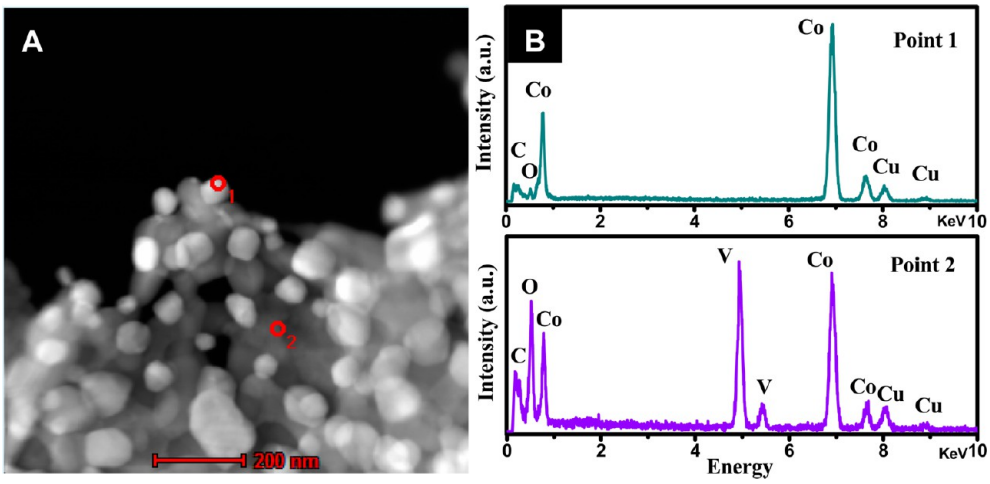

Figure 13. EDS studies of the $Co_3V_2O_8$ nanosheet (12 h) electrodes collected at a cutoff voltage of 0.01 V when discharged at a high current density of 1 A g^{-1}. EDS spectra in (B) correspond to points 1 and 2 marked in red circles in (A) the STEM image.

with the increasing number of cycles, as shown in Figure 6A. Anomalous behaviors have been reported in previous reports.[29] Two factors may be attributed to this phenomenon: (1) the multilayered $Co_3V_2O_8$ nanosheets have transformed into CoO as the lithium ions insert in the first discharge process, while the deconstruction of the crystal $Co_3V_2O_8$ and emergence of lithiated amorphous $Li_xV_2O_5$ may lower the conductivity of the electrodes, which will synergistically affect the lithium storage and cause capacity fading at the early stage; (2) just as mentioned above, the remaining unused active materials would be further pulverized into finer Co quantum dots, which continually increases active sites as the lithium ions insert, resulting in an increased capacity with the increasing number of cycles. It can be predicted that if more cycles are applied in the cycling performance for our multilayered $Co_3V_2O_8$ nanosheets, the capacity will reach a maximum and then drop,

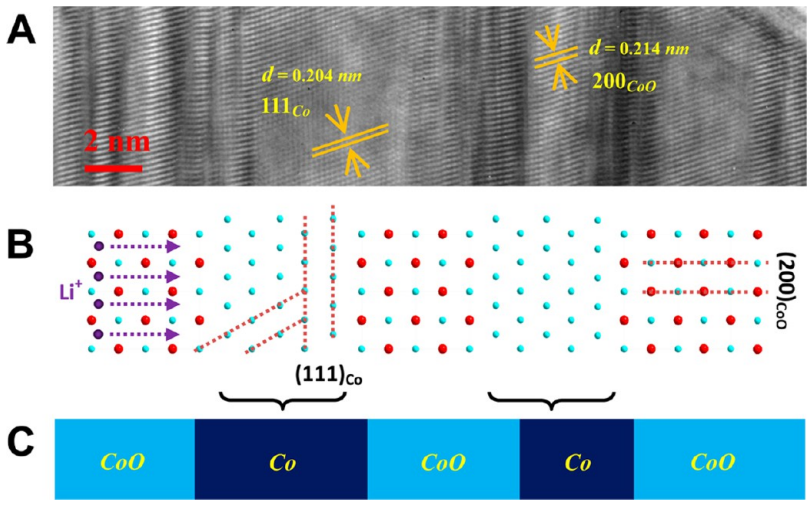

Figure 14. (A) HRTEM image of an individual nanoparticle collected at a cutoff voltage of 0.01 V when discharged at a high current density of 1 A g^{-1}. (B) Structural illustration of the atomic model corresponding to the HRTEM in (A). (C) Schematic representation of the most probable electrode morphology.

due to the full usage of active materials and the decreasing conductivity upon later cycling.

CONCLUSIONS

In summary, we have reported for the first time the successful preparation of $Co_3V_2O_8$ nanosheets via a simple hydrothermal method followed by annealing in air at 350 °C for 2 h. The as-synthesized products exhibit unique multilayered structures constructed from the self-assembly of the exfoliated ultrathin nanosheets that are accompanied by the emergence of channel voids of 4 nm. When tested as anode materials for lithium batteries, the multilayered $Co_3V_2O_8$ nanosheets show excellent performances of Li storage. Under the condition of a high current density of 1 A g^{-1}, the multilayered $Co_3V_2O_8$ nanosheets are capable of retaining a specific capacity of 1114 mA h g^{-1} over 100 cycles. Even when cycled at 5 and 10 A g^{-1}, comparable capacities of 525 and 361 mA h g^{-1} could still be achieved, indicating a superior rate capability.

By the close TEM measurements, one plausible mechanism has been proposed to address the electrochemical behaviors of the multilayered $Co_3V_2O_8$ nanosheets. The results reveal that the lithium intercalation into the $Co_3V_2O_8$ mainly involves the conversion reaction between CoO and Co that occurs on the amorphous lithiated vanadium oxide nanosheets. On the basis of the above analyses, the outstanding electrochemical performances of the multilayered $Co_3V_2O_8$ nanosheets at both low and large current densities should be ascribed to the following points: (1) the surplus interfaces generated during the material growth can increase the surface area that is favorable to the infiltration of electrolyte and benefits the available space for lithium ion diffusion; (2) the unique architectures among the lithium intercalations effectively prohibit the agglomerations of the nanoparticles and consequently will keep the multilayered nanostructures; (3) superior to single-phase oxides, the strongly coupled mixed-metal oxides may synergistically enhance the electrochemical properties such as electrical/ionic conductivity, reversible capacity, and mechanical stability. Thus, the novel multilayered $Co_3V_2O_8$ nanosheets show great promise as anodes for lithium ion batteries.

EXPERIMENTAL SECTION

Synthesis and Characterization. In a typical synthesis, 187 mg (50 mmol L^{-1}) of NH_4VO_3 (Sigma-Aldrich, 99%) was dissolved into 32 mL of deionized water at 80 °C. Under severe stirring, 40 mg (30 mmol L^{-1}) of $LiOH·H_2O$ (Sigma-Aldrich, 99%) was added to the ammonium metavanadate solution. Then, 76 mg of $CoCl_2·6H_2O$ (Sigma-Aldrich, 98%) was added to the solution under stirring. After continuous stirring for 10 min, the resulting yellow precursor suspension was transferred into a 40 mL Teflon-lined autocalve and maintained at 180 °C for 12 h. After being cooled to ambient temperature naturally, the brown powders in the autocalve were collected by centrifugation, washed with deionized water, followed by absolute ethanol three times, and dried at 80 °C for 6 h. Finally, all the products were calcined in air at 350 °C for 2 h with a heating rate of 2 °C min^{-1} to obtain highly crystalline powders.

The product morphology was examined using a field-emitting scanning electron microscope (FESEM; JEOL, JSM-6700F, 15 kV). TEM images were obtained using a FEI F30 microscope at an operating voltage of 300 kV. XRD analysis was performed on a D/Max 2500 (Rigaku Co., Japan) using Cu Kα radiation at a generator voltage of 40 kV and a generator current of 30 mA with a scanning speed of 2 deg min^{-1}. AFM images of the products on a fresh silicon surface were taken with a Nanoscope III in tapping mode using an NSC14/no Al probe (MikroMash, Wislsonville, OR, USA). XPS measurements were conducted with two separate systems equipped with monochromatic Al K sources (ESCALab 250, USA) to analyze the chemical compositions of the products. The N_2 adsorption experiments using an ASAP 2020 surface area analyzer (Micrometeritics Co., USA) were conducted to investigate the porosity of the products. The specific surface area of the samples was calculated

according to the Brunauer–Emmett–Teller equation from the adsorption data.

Electrochemical Characterization. The working electrode was fabricated by mixing of active material (*e.g.*, $Co_3V_2O_8$ nanosheets), a conductive agent (Super-P, Sigma-Aldrich), and a sodium alginate (SA, Sigma-Aldrich) in a weight ratio of 70:20:10. Then, the mixture was coated on a copper foil (d_{Cu} = 18 μm). After drying in air at 90 °C for 6 h, the electrodes were assembled into coin-like cells (CR2032) with pure lithium metal as both the counter electrode and the reference electrode. The electrolyte used was 1.0 M in a 50:50 (w/w) mixture of ethylene carbonate and diethyl carbonate solution. The total mass of the electrode materials is *ca.* 1.5–1.8 mg, measured by an ultramicro analytical balance (Mettle Toledo XP2U, 0.1 μg resolution), while the mass of the active material (multilayered $Co_3V_2O_8$ nanosheets) is *ca.* 1.0–1.2 mg. Cell assembly was carried out in an Ar (99.999%)-filled glovebox (Mikrouna Co., Ltd. Universal). Cyclic voltammetry (0.01–2.5 V, 0.2 mV s^{-1}) was performed using an electrochemical workstation (IM6e-X). The charge/discharge tests were performed using a NEWARE battery tester at different current rates with a voltage window of 0.01–2.5 V.

Conflict of Interest: The authors declare no competing financial interest.

Acknowledgment. This work was financially supported by the National Natural Science Foundation of China (No. 51125008 and No. 11274392).

Supporting Information Available: Morphological and structural studies of $Co_3V_2O_8 \cdot nH_2O$ nanosheets. TEM analyses of the $Co_3V_2O_8$ nanosheet (12 h) electrodes collected at different cutoff voltages. XPS spectra of the freshly prepared electrode, reduced electrode, and reoxidized electrode when discharged at a high current density of 1 A g^{-1}. Precise description of the CoO/Co interfaces and schematic diagram of the possible electrochemical reactions between lithium ions and $Co_3V_2O_8$ nanosheets. This material is available free of charge *via* the Internet at http://pubs.acs.org.

REFERENCES AND NOTES

1. Poizot, P.; Laruelle, S.; Grugeon, S.; Dupont, L.; Tarascon, J. M. Nano-Sized Transition-Metaloxides as Negative-Electrode Materials for Lithium-Ion Batteries. *Nature* **2000**, *407*, 496–499.
2. Taberna, L.; Mitra, S.; Poizot, P.; Simon, P.; Tarascon, J. M. High Rate Capabilities Fe_3O_4-Based Cu Nano-Architectured Electrodes for Lithium-Ion Battery Applications. *Nat. Mater.* **2006**, *5*, 567–573.
3. Arico, A. S.; Bruce, P.; Scrosati, B.; Tarascon, J. M. Nanostructured Materials for Advanced Energy Conversion and Storage Devices. *Nat. Mater.* **2005**, *4*, 366–377.
4. Nam, K. T.; Kim, D. W.; Yoo, P. J.; Chiang, C. Y.; Meethong, N.; Hammond, P. T.; Chiang, Y. M.; Belcher, A. M. Virus-Enabled Synthesis and Assembly of Nanowires for Lithium Ion Battery Electrodes. *Science* **2006**, *312*, 885–888.
5. Reddy, M. V.; Rao, G. V. S.; Chowdari, B. V. R. Metal Oxides and Oxysalts as Anode Materials for Li Ion Batteries. *Chem. Rev.* **2013**, *113*, 5364–5457.
6. Sim, D. H.; Rui, X. H.; Chen, J.; Tan, H. T.; Lim, T. M.; Yazami, R.; Hng, H. H.; Yan, Q. Y. Direct Growth of $FeVO_4$ Nanosheet Arrays on Stainless Steel Foil as High-Performance Binder-Free Li Ion Battery Anode. *RSC Adv.* **2012**, *2*, 3630–3633.
7. Bruce, P. G.; Scrosati, B.; Tarascon, J. M. Nanomaterials for Rechargeable Lithium Batteries. *Angew. Chem., Int. Ed.* **2008**, *47*, 2930–2946.
8. Zhang, Q. F.; Uchaker, E.; Candelaria, S. L.; Cao, G. Z. Nanomaterials for Energy Conversion and Storage. *Chem. Soc. Rev.* **2013**, *42*, 3127–3171.
9. Liu, C.; Li, F.; Ma, L. P.; Cheng, H. M. Advanced Materials for Energy Storage. *Adv. Mater.* **2010**, *22*, 28–62.
10. Son, M. Y.; Hong, Y. J.; Kang, Y. C. Superior Electrochemical Properties of Co_3O_4 Yolk-Shell Powders with A Filled Core and Multishells Prepared by A One-Pot Spray Pyrolysis. *Chem. Commun.* **2013**, *49*, 5678–5680.
11. Zhang, X. F.; Song, X. X.; Gao, S.; Xu, Y. M.; Cheng, X. L.; Zhao, H.; Huo, L. H. Facile Synthesis of Yolk-Shell MoO_2 Microspheres with Excellent Electrochemical Performance as a Li-Ion Battery Anode. *J. Mater. Chem. A* **2013**, *1*, 6858–6864.
12. Pan, A. Q.; Wu, H. B.; Zhang, L.; Lou, X. W. Uniform V_2O_5 Nanosheet-Assembled Hollow Microflowers with Excellent Lithium Storage Properties. *Energy Environ. Sci.* **2013**, *6*, 1476–1479.
13. Liu, J. H.; Chen, J. S.; Wei, X. F.; Lou, X. W. Sandwich-Like, Stacked Ultrathin Titanate Nanosheets for Ultrafast Lithium Storage. *Adv. Mater.* **2011**, *23*, 998–1002.
14. Zhou, J. S.; Song, H. H.; Chen, X. H.; Zhi, L. J.; Yang, S. Y.; Huo, J. P.; Yang, W. T. Carbon-Encapsulated Metal Oxide Hollow Nanoparticles and Metal Oxide Hollow Nanoparticles: A General Synthesis Strategy and Its Application to Lithium-Ion Batteries. *Chem. Mater.* **2009**, *21*, 2935–2940.
15. Shen, L. F.; Li, H. S.; Uchaker, E.; Zhang, X. G.; Cao, G. Z. General Strategy for Designing Core-Shell Nanostructured Materials for High-Power Lithium Ion Batteries. *Nano Lett.* **2012**, *12*, 5673–5678.
16. Reddy, A. L. M.; Shaijumon, M. M.; Gowda, S. R.; Ajayan, P. M. Coaxial MnO_2/Carbon Nanotube Array Electrodes for High-Performance Lithium Batteries. *Nano Lett.* **2009**, *9*, 1002–1006.
17. Yang, G. Z.; Song, H. W.; Cui, H.; Liu, Y. C.; Wang, C. X. Ultrafast Li-Ion Battery Anode with Superlong Life and Excellent Cycling Stability from Strongly Coupled ZnO Nanoparticle/Conductive Nanocarbon Skeleton Hybrid Materials. *Nano Energy* **2013**, *2*, 579–585.
18. Rolison, D. R.; Long, J. W.; Lytle, J. C.; Fischer, A. E.; Rhodes, C. P.; McEvoy, T. M.; Bourga, M. E.; Lubers, A. M. Multifunctional 3D Nanoarchitectures for Energy Storage and Conversion. *Chem. Soc. Rev.* **2009**, *38*, 226–252.
19. Gowda, S. R.; Reddy, A. L. M.; Zhan, X. B.; Jafry, H. R.; Ajayan, P. M. 3D Nanoporous Nanowire Current Collectors for Thin Film Microbatteries. *Nano Lett.* **2012**, *12*, 1198–1202.
20. Huang, Y. S.; Wu, D. Q.; Han, S.; Li, S.; Xiao, L.; Zhang, F.; Feng, X. L. Assembly of Tin Oxide/Graphene Nanosheets into 3D Hierarchical Frameworks for High-Performance Lithium Storage. *CHEMSUSCHEM* **2013**, *6*, 1510–1515.
21. Wu, Z. S.; Ren, W. C.; Wen, L.; Gao, L. B.; Zhao, J. P.; Chen, Z. P.; Zhou, G. M.; Li, F.; Cheng, H. M. Graphene Anchored with Co_3O_4 Nanoparticles as Anode for Lithium Ion Batteries with Enhanced Reversible Capacity and Cyclic Performance. *ACS Nano* **2010**, *4*, 3187–3194.
22. Li, X. F.; Meng, X. B.; Liu, J.; Geng, D. S.; Zhang, Y.; Banis, M. N.; Li, Y. L.; Yang, J. L.; Li, R. Y.; Sun, X. L. Tin Oxide with Controlled Morphology and Crystallinity by Atomic Layer Deposition onto Graphene Nanosheets for Enhanced Lithium Storage. *Adv. Funct. Mater.* **2012**, *22*, 1647–1654.
23. Zou, Y. Q.; Wang, Y. Sn@CNT Nanostructures Rooted in Graphene with High and Fast Li-Storage Capacities. *ACS Nano* **2011**, *5*, 8108–8114.
24. Luo, B.; Wang, B.; Li, X. L.; Jia, Y. Y.; Liang, M. H.; Zhi, L. J. Graphene-Confined Sn Nanosheets with Enhanced Lithium Storage Capability. *Adv. Mater.* **2012**, *24*, 3538–3543.
25. Su, Y. Z.; Li, S.; Wu, D. Q.; Zhang, F.; Liang, H. W.; Gao, P. F.; Cheng, C.; Feng, X. L. Two-Dimensional Carbon-Coated Graphene/Metal Oxide Hybrids for Enhanced Lithium Storage. *ACS Nano* **2012**, *6*, 8349–8356.
26. Song, H. W.; Li, N.; Cui, H.; Wang, C. X. Enhanced Capability and Cyclability of SnO_2-Graphene Oxide Hybrid Anode by Firmly Anchored SnO_2 Quantum Dots. *J. Mater. Chem. A* **2013**, *1*, 7558–7562.
27. Jin, S. X.; Li, N.; Cui, H.; Wang, C. X. Growth of the Vertically Aligned Graphene@Amorphous GeO_x Sandwich Nanoflakes and Excellent Li Storage Properties. *Nano Energy* **2013**, *2*, 1128–1136.
28. Yang, S. B.; Feng, X. L.; Mullen, K. Sandwich-Like, Graphene-Based Titania Nanosheets with High Surface Area for Fast Lithium Storage. *Adv. Mater.* **2011**, *23*, 3575–3579.
29. Peng, C. X.; Chen, B. D.; Qin, Y.; Yang, S. H.; Li, C. Z.; Zuo, Y. H.; Liu, S. Y.; Yang, J. H. Facile Ultrasonic Synthesis of CoO Quantum Dot/Graphene Nanosheet Composites with High Lithium Storage Capacity. *ACS Nano* **2012**, *6*, 1074–1081.

30. Yu, L.; Zhang, L.; Wu, H. B.; Zhang, G. Q.; Lou, X. W. Controlled Synthesis of Hierarchical $Co_xMn_{3-x}O_4$ Array Micro-/Nanostructures with Tunable Morphology and Composition as Integrated Electrodes for Lithium-Ion Batteries. *Energy Environ. Sci.* **2013**, *6*, 2664–2671.
31. Sharma, Y.; Sharma, N.; Rao, G. V. S.; Chowdari, B. V. R. Nanophase $ZnCo_2O_4$ as a High Performance Anode Material for Li-Ion Batteries. *Adv. Funct. Mater.* **2007**, *17*, 2855–2861.
32. Cherian, C. T.; Sundaramurthy, J.; Reddy, M. V.; Kumar, P. S.; Mani, K.; Pliszka, D.; Sow, C. H.; Ramakrishna, S.; Chowdari, B. V. R. Morphologically Robust $NiFe_2O_4$ Nanofibers as High Capacity Li-Ion Battery Anode Material. *ACS Appl. Mater. Interfaces* **2013**, *5*, 9957–9963.
33. Denis, S.; Baudrin, E.; Orsini, F.; Ouvrard, G.; Touboul, M.; Tarascon, J. M. Synthesis and Electrochemical Properties of Numerous Classes of Vanadates. *J. Power Sources* **1999**, *81–82*, 79–84.
34. Baudrin, E.; Laruelle, S.; Denis, S.; Touboul, M.; Tarascon, J. M. Synthesis and Electrochemical Properties of Cobalt Vanadates *vs.* Lithium. *Solid State Ionics* **1999**, *123*, 139–153.
35. Yang, T.; Xia, D. G.; Wang, Z. L.; Chen, Y. A Novel Anode Material of Fe_2VO_4 for High Power Lithium Ion Battery. *Mater. Lett.* **2009**, *63*, 5–7.
36. Sun, Y.; Li, C. S.; Wang, L. N.; Wang, Y. Z.; Ma, X. G.; Ma, P. J.; Song, M. Y. Ultralong Monoclinic ZnV_2O_6 Nanowires: Their Shape-Controlled Synthesis, New Growth Mechanism, and Highly Reversible Lithium Storage in Lithium-Ion Batteries. *RSC Adv.* **2012**, *2*, 8110–8115.
37. Zeng, L. X.; Xiao, F. Y.; Wang, J. C.; Gao, S. K.; Ding, X. K.; Wei, M. D. ZnV_2O_4-CMK Nanocomposite as an Anode Material for Rechargeable Lithium Ion Batteries. *J. Mater. Chem.* **2012**, *22*, 14284–14288.
38. Wei, M. D.; Sugihara, H.; Honma, I.; Ichihara, M.; Zhou, H. S. A New Metastable Phase of Crystallized $V_2O_4 \cdot 0.25H_2O$ Nanowires: Synthesis and Electrochemical Measurements. *Adv. Mater.* **2005**, *17*, 2964–2969.
39. Li, B. X.; Xu, Y.; Rong, G. X.; Jing, M.; Xie, Y. Vanadium Pentoxide Nanobelts and Nanorolls: From Controllable Synthesis to Investigation of Their Electrochemical Properties and Photocatalytic Activities. *Nanotechnology* **2006**, *17*, 2560–2566.
40. Ma, H.; Zhang, S. Y.; Ji, W. Q.; Tao, Z. L.; Chen, J. Alpha-CuV_2O_6 Nanowires: Hydrothermal Synthesis and Primary Lithium Battery Application. *J. Am. Chem. Soc.* **2008**, *130*, 5361–5367.
41. Ryu, W. H.; Shin, J.; Jung, J. W.; Kim, I. D. Cobalt(II) Monoxide Nanoparticles Embedded in Porous Carbon Nanofibers as a Highly Reversible Conversion Reaction Anode for Lithium Ion Batteries. *J. Mater. Chem. A* **2013**, *1*, 3239–3243.
42. Xiong, S. L.; Chen, J. S.; Lou, X. W.; Zeng, H. C. Mesoporous Co_3O_4 and CoO@C Topotactically Transformed from Chrysanthemum-Like $Co(CO_3)0.5(OH) \cdot 0.11H_2O$ and Their Lithium-Storage Properties. *Adv. Funct. Mater.* **2012**, *22*, 861–871.
43. Wang, X.; Cao, X. Q.; Bourgeois, H.; Guan, H.; Chen, S. M.; Zhong, Y. T.; Tang, D. M.; Li, H. Q.; Zhai, T. Y.; Li, L.; *et al.* N-Doped Graphene-SnO_2 Sandwich Paper for High-Performance Lithium-Ion Batteries. *Adv. Funct. Mater.* **2012**, *22*, 2682–2690.
44. Zhang, L.; Wu, H. B.; Madhavi, S.; Hng, H. H.; Lou, X. W. Formation of Fe_2O_3 Microboxes with Hierarchical Shell Structures from Metal-Organic Frameworks and Their Lithium Storage Properties. *J. Am. Chem. Soc.* **2012**, *134*, 17388–17391.
45. Chen, J.; Xu, L. N.; Li, W. Y.; Gou, X. L. Alpha-Fe_2O_3 Nanotubes in Gas Sensor and Lithium-Ion Battery Applications. *Adv. Mater.* **2005**, *17*, 582–586.
46. Hu, J.; Li, H.; Huang, X. J.; Chen, L. Q. Improve the Electrochemical Performance of Cr_2O_3 Anode for Lithium Ion Batteries. *Solid State Ionics* **2006**, *177*, 2791–2799.
47. Dalverny, A. L.; Filhol, J. S.; Doublet, M. L. Interface Electrochemistry in Conversion Materials for Li-Ion Batteries. *J. Mater. Chem.* **2011**, *21*, 10134–10142.